Journal of Engineering Mechanics and Machinery (2024)
Clausius Scientific Press, Canada

DOI: 10.23977/jemm.2024.090116
ISSN 2371-9133 Vol. 9 Num. 1

Optimization of bandgaps for phononic crystal plate with protrusions based on adaptive genetic algorithm

Ni Zhen[1,a,*], Rurui Huang[1,b], Wanpeng Wu[1,c]

[1]*School of Mechanical Engineering, Tianjin University of Science and Technology, Tianjin, 300222, China*
[a]*zhenni@tust.edu.cn*, [b]*huangrr1999@163.com*, [c]*2944622471@qq.com*
[*]*Corresponding author*

Keywords: Adaptive genetic algorithm, bandgap characteristic, optimal design, phononic crystal thin plate with protrusion

Abstract: In this paper, phononic crystal plates with spherical, square, and cylindrical protrusions are designed. The band structures of phononic crystal plates with one-side and double-side protrusions are calculated using the finite element method. Under the same set of all parameters, the relative bandgap widths with square and cylindrical protrusions are larger, and the volume with spherical protrusions is smaller. Next, the influences of geometric and material parameters on the relative bandgap width are discussed to determine the decision variable and optimization interval. Finally, an adaptive genetic algorithm is applied to optimize the design of bandgap characteristics and lightweight design. The frequency response curves of the optimized structure are also calculated to verify the accuracy and efficiency of the optimization model. The results show that the relative bandgap width of the phononic crystal plate is enlarged greatly with a slightly increased volume of protrusion for the optimized structure. The study can provide a new idea for applying lightweight phononic crystal plates in vibration damping.

1. Introduction

Phononic crystals have developed rapidly in the past few decades. A lot of excellent characteristics are presented in pioneer work, such as negative refractive [1-4], defect state [5-7], phononic bandgap [8-13], slow wave effect, etc., which is similar to the propagation of electrons and electromagnetic waves in natural crystals and photonic crystals. The phononic bandgap due to the mechanisms of Bragg scattering [14] or local resonance [15] is one of the most distinguished features of phononic crystals, which can be applied in vibration damping and noise reduction [16-18]. In addition, plate structures are widely used in machine manufacturing, automobiles, aerospace, civil engineering, electronic components, etc., which generate and transmit vibration easily. The vibration on plate structures can result in resonance and fatigue and then intensify the failure of structures [19].

The bandgap characteristic of phononic crystal is introduced into plate structures to reduce the effect of vibration on a plate. The phononic crystal plates (PCPs) have attracted widespread attention, and many related studies have been presented [20-25]. The added protrusions in PCPs are first presented in [26] and [27]. Zhao et al. [28] proposed a double-vibrator three-component pillared

phononic crystal plate and theoretically studied the properties. Li et al. [29] studied the phononic structure bands containing periodic elliptical inclusions in a square lattice using the plane wave expansion method. Yu et al. [30] numerically investigated the elastic wave propagation in two-dimensional phononic crystals composed of an array of steel stepped resonators on a rubber slab. Since the local resonance, phononic crystals with protrusions are not restricted to the size of the periodic structure to a certain extent, they can obtain a low-frequency vibration bandgap, and the wavelength corresponding to the frequency is two orders of magnitude larger than the lattice constant. On the other hand, the protrusions increase the thickness of the phononic crystal plate, which results in the applications of PCPs needing to be expanded due to geometric size and the increase of materials. Researchers try to seek thin and lightweight PCPs as vibration-damping materials. The optimization of PCPs, taking into account the lower-frequency broadband and smaller thickness simultaneously, has become a hot topic [31-33].

With the development of intelligent optimization algorithms [34], this problem can be well solved. An adaptive genetic algorithm (AGA) is a heuristic algorithm that can implement random search referring to the mechanisms of natural selection and genetics in the biological world [35, 36]. AGA is particularly good at searching for solutions to problems involving large search spaces. The probability of crossover and mutation can be controlled flexibly based on the self-adaption of AGA. Then, the optimal individual of the current generation is not destroyed, and the better individual must correspond to a higher probability of crossover and mutation.

This paper proposes PCPs with spherical, square, and cylindrical protrusions. The material of the protrusions is the same as the scatterers embedded in a matrix plate in a square lattice. The band structures of PCPs with protrusions are numerically calculated by COMSOL software. The results show that PCPs with protrusions can enhance the effect of local resonance between scatterers and matrix and obtain lower frequency band gaps. The effects of geometrical and material parameters on band structures of PCPs with three different protrusions are discussed in detail. The optimization intervals of important parameters are determined. Then, the optimal models of the PCPs with three different protrusions are established using AGA. Finally, the accuracy and efficiency of the optimized structures are verified by the frequency response curves. The analyses indicate that optimizing bandgaps for PCPs with protrusions can obtain lower bandgaps and achieve a smaller plate thickness for lightweight design.

2. Structural design and simulation

2.1. The structures of PCPs with protrusions

The schematic diagram of PCPs with spherical protrusions is shown in Figure 1. The domain enclosed by dotted lines in Figure 1(a) represents a unit cell of the PCPs with a spherical protrusion in a square lattice. The blue-colored part is the protrusion, which has the same bottom area as the cylindrical scatterer. One-side and double-side protrusions are added on the upper and lower surfaces of the PCPs. The lattice constant is a=8 mm, the height of the plate is h=0.5 mm, and the bottom area of the protrusion is S=28.27 mm^2. The height of the protrusion is always the same as h. The material of the matrix is rubber with Young's modulus E_0=1.175×10^5 Pa, mass density ρ_0=1300 kg·m^{-3}, and Poisson's ratio v_0=0.47. The material of scatterers is steel with Young's modulus E_1=2×10^{11} Pa, mass density ρ_1=7850 kg·m^{-3}, and Poisson's ratio v_1=0.33. PCPs with square and cylindrical protrusions are shown in Figure 1(b) and Figure 1(a), respectively. For the two structures, all geometric and material parameters are the same as those in Figure 1(a).

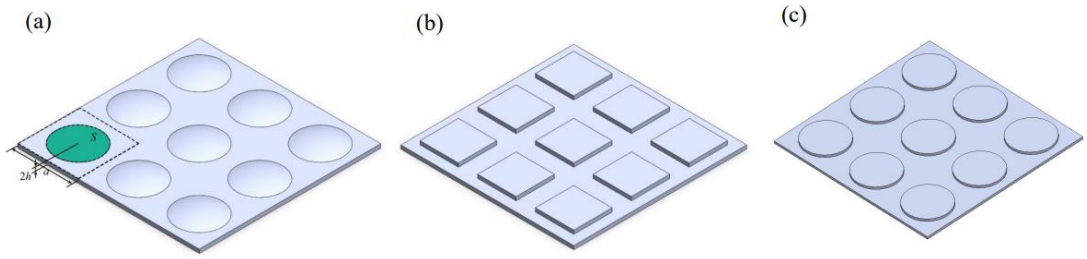

Figure 1: (a) Schematic diagram of PCPs with spherical, (b) square, and (c) cylindrical protrusions.

The plate has two vibration modes, including longitudinal vibration parallel to the plate surface and bending vibration perpendicular to the plate surface. The longitudinal vibration wave equation in the plate is expressed as follows:

$$\rho \frac{\partial^2 u_y}{\partial t^2} = \frac{\partial \sigma_y}{\partial y} + \frac{\partial \tau_{yx}}{\partial x}, \tag{1}$$

$$\rho \frac{\partial^2 u_x}{\partial t^2} = \frac{\partial \sigma_x}{\partial x} + \frac{\partial \tau_{xy}}{\partial y}, \tag{2}$$

Equation of motion of bending vibration is:

$$-\chi \frac{\partial^2 u_z}{\partial t^2} = \frac{\partial^2}{\partial x^2}(D\frac{\partial^2 u_z}{\partial x^2} + \xi \frac{\partial^2 u_z}{\partial y^2}) + 2\frac{\partial^2}{\partial x \partial y}(\gamma \frac{\partial^2 u_z}{\partial x \partial y}) + \frac{\partial^2}{\partial y^2}(D\frac{\partial^2 u_z}{\partial y^2} + \xi \frac{\partial^2 u_z}{\partial x^2}) \tag{3}$$

Where ρ, E and v are the mass density, Young's modulus and Poisson's ratio, respectively; $D=Eh^3/12(1-v^2)$, $\chi=\rho h$, $\xi=Dv$ and $\gamma=D(1-v)$ are periodic functions related to the position vector $\boldsymbol{r}=[x, y]^T$, u_x and u_y are the displacement components of the displacement vector $\boldsymbol{u}=[u_x, u_y]^T$ along the x, y direction.

Due to the periodicity of phononic crystals, one unit cell can be selected to solve the wave equation in finite element software. The discrete eigenvalue equation of one unit cell in a phononic crystal plate can be written as:

$$\boldsymbol{K}\boldsymbol{u} = \omega^2 \boldsymbol{M}\boldsymbol{u}, \tag{4}$$

Where $\boldsymbol{K}$ and $\boldsymbol{M}$ are the stiffness matrix and mass matrix of the structure, respectively.

In the finite element software COMSOL, the unit cell models of the PCPs with three different protrusions are established. According to the Bloch theorem, in a periodic composite structure, one unit cell can be selected for the calculation of the displacement. The boundary conditions can be expressed as the following equations on the four edges of the square unit cell.

$$\boldsymbol{u}(x+a, y) = \boldsymbol{u}(x, y)e^{ik_x \cdot a} \tag{5}$$

$$\boldsymbol{u}(x, y+a) = \boldsymbol{u}(x, y)e^{ik_y \cdot a} \tag{6}$$

Where $\boldsymbol{k}=[k_x, k_y]$ is the Bloch wave vector.

Next, parametric scanning along the boundaries of the first Brillouin zone is implemented in COMSOL. The Brillouin boundary is shown in Figure 2(a). From M to Γ, $k_x=(1-\eta)\pi/a$, $k_y=(1-\eta)\pi/a$, where η changes from 0 to 1; From Γ to X, $k_x=(\eta-1)\pi/a$, $k_y=0$, where η changes from 1 to 2; From X to M, $k_x=\pi/a$, $k_y=(\eta-2)\pi/a$, where η changes from 2 to 3.

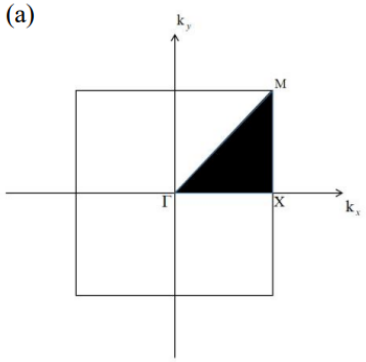

Figure 2: (a) The first Brillouin zone.

The band structures of PCPs with one-sided spherical, square, and cylindrical protrusions are shown in Figure 3(a), (b), and (c), respectively. The range of bandgaps, relative bandgap width, and the volume of protrusion are listed in Table 1 for each situation. For comparison, the thickness of the PCPs without protrusion is set at 2 h, equal to the total thickness of PCPs with protrusions. It can be found that the PCPs with one-sided protrusions can obtain lower frequency and larger width of bandgaps. In addition, the sum of the first and second bandgap of the PCPs with square and cylindrical protrusions is larger than that of PCPs with spherical protrusions. However, the volume of the spherical protrusion is only about half that of the square and cylindrical protrusion, which favors lightweight.

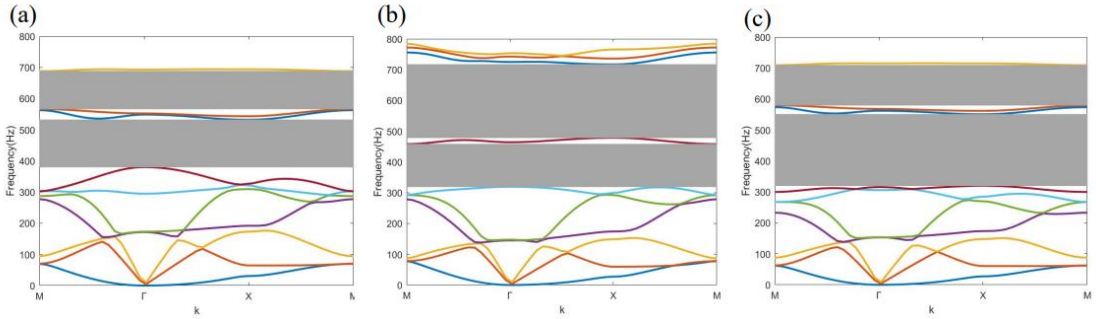

Figure 3: Band structures of the PCPs with one side (a) spherical, (b) square, and (c) cylindrical protrusions.

Table 1: Bandgaps of the PCPs with one-side protrusions.

Protrusion type	First bandgap frequency range (hz)/relative bandgap width	Second bandgap frequency range (hz)/relative bandgap width	The sum of the relative bandgap width	Protrusion volume (mm^3)
Without protrusion	500-750/0.26	825-930/0.12	0.38	32
Square	320-460/0.36	480-715/0.39	0.75	14.124
Sphere	375-535/0.35	570-690/0.19	0.54	7.1313
Cylinder	320-550/0.53	580-710/0.2	0.73	14.124

Similarly, the band structures of PCPs with double-side protrusions for the three geometric shapes are also calculated, as shown in Figure 4. The range of bandgaps, relative bandgap width, and the volume of protrusion are listed in Table 2. It can be found that the PCPs with double-side protrusions can also obtain lower frequency and larger width of bandgaps. By comparing Table 1 and Table 2,

PCPs with double-side protrusions can achieve lower frequency and larger width of bandgaps than one-side protrusions due to the thickness being 3*h*.

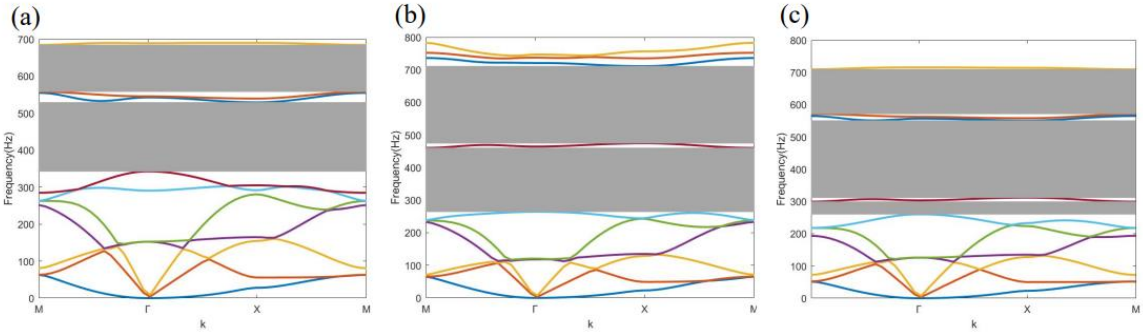

Figure 4: Band structures of the PCPs with double-side (a) spherical, (b) square, and (c) cylindrical protrusions.

Table 2: Bandgaps of the PCPs with double-side protrusions.

Protrusion type	First bandgap frequency range (hz)/relative bandgap width	Second bandgap frequency range (hz)/relative bandgap width	The sum of the relative bandgap width	Protrusion volume (mm^3)
Without protrusion	420-510/0.19	600-850/0.34	0.53	64
Square	260-460/0.56	475-710/0.4	0.96	28.248
Sphere	340-530/0.44	570-690/0.19	0.63	14.2626
Cylinder	315-550/0.54	575-710/0.21	0.75	28.248

2.2. Influence of geometric and material parameters on band structures

The influences of the geometrical shape of the protrusion with the same height, bottom area, and materials on the bandgap characteristics are discussed above. In this subsection, the geometric and material parameters are changed to analyze the effect of these factors on band structures, including height, bottom area, mass density, Young's modulus, and Poisson's ratio of the protrusions.

With other parameters unchanged, only the height or the bottom area of the protrusion gets changed. The variation of relative bandgap width with bottom area for PCPs with one-side and double-side protrusions are shown in Figure 5(a) and (b), respectively; the variation of relative bandgap width with height of protrusion for PCPs with one-side and double-side protrusions are shown in Figure 5(c) and (d), respectively. The relative bandgap width is the sum of the first and second relative bandgap width. It can be seen that the results for one-side protrusion and double-side protrusion are almost the same. The relative bandgap widths for square protrusion are close to those for cylindrical protrusions due to the same volume of protrusions. The relative bandgap widths are enlarged as the increase of both the bottom area and height of protrusion. The relative bandgap width for spherical and cylindrical protrusions will reach a maximum at the bottom area of protrusion over about 40 mm^2 and then decrease. The maximum relative bandgap width cannot be directly determined, so the effective design interval of the bottom area of the protrusion for PCPs with one-side and double-side spherical and cylindrical protrusions is selected in a range close to 40 mm^2.

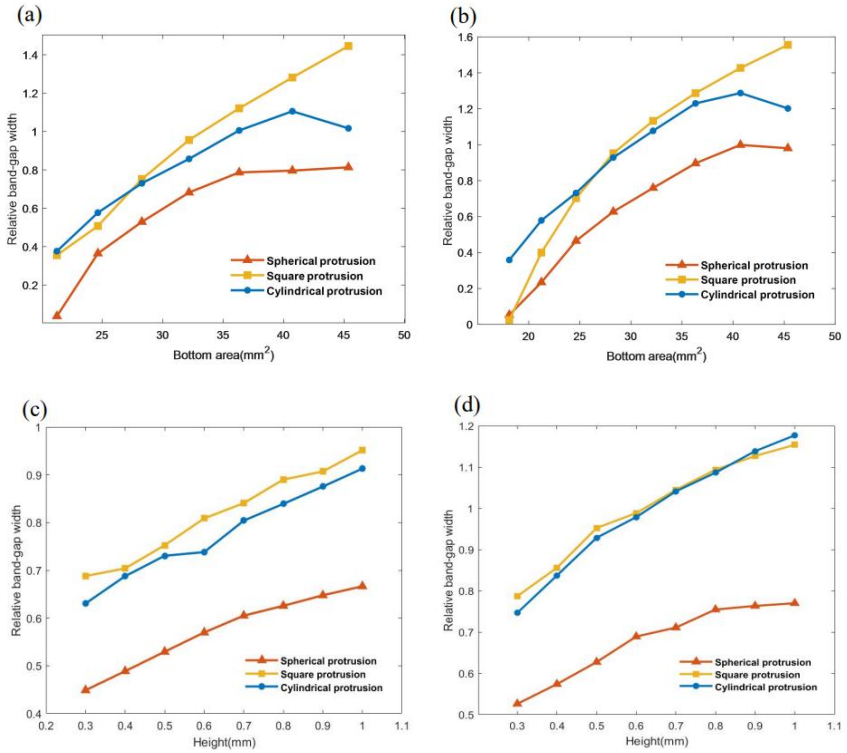

Figure 5: Variation of relative bandgap width with bottom area of the protrusion for PCPs with (a) one-side and (b) double-side protrusions; variation of relative bandgap width with height of the protrusion for PCPs with (c) one-side and (d) double-side protrusions.

The influences of the material parameters of scatterers on bandgaps are also analyzed. The variations of the sum of the first and second relative bandgap width with mass density, Young's modulus, and Poisson's ratio of scatterer are shown in Figure 6(a)~(f). It can be seen that the results for the one-side protrusion are in agreement with those for the double-side protrusion. For all three types of protrusions, the relative bandgap widths increase with the increase of mass density of the scatterer but are weakly affected by Young's modulus and Poisson's ratio of the scatterer. Therefore, it is unnecessary to consider Young's modulus and Poisson's ratio of scatterer materials when selecting materials. High mass density is in favor of larger relative bandgap width.

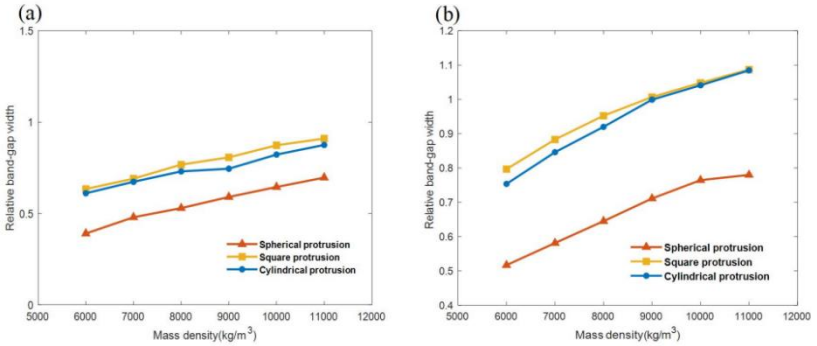

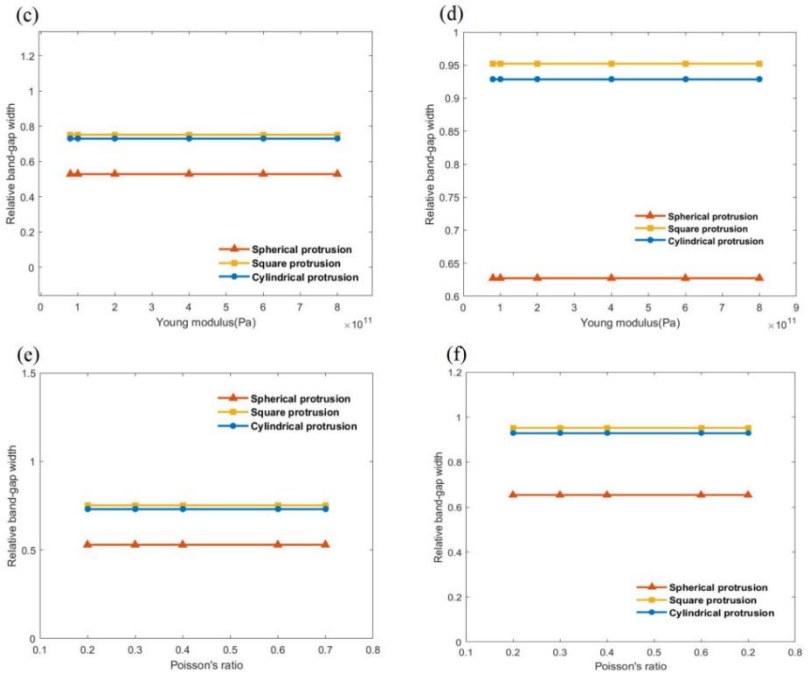

Figure 6: Variation of relative bandgap width with mass density of the scatterer for PCPs with (a) one-side and (b) double-side protrusions; variation of relative bandgap width with Young's modulus of the scatterer for PCPs with (c) one-side and (d) double-side protrusions; variation of relative bandgap width with Poisson's ratio of the scatterer for PCPs with (e) one-side and (f) double-side protrusions.

2.3. Optimization of bandgaps for PCPs with protrusions

According to the above analysis, both the larger height of protrusion and the larger mass density of the scatterer will generate larger relative bandgap width for the three protrusions. The relative bandgap width of PCPs with square protrusions also gets enlarged with the increase of the bottom area of protrusion. However, the relative bandgap widths of PCPs with spherical and cylindrical protrusions increase first and then decrease as the bottom area of protrusion exceeds a certain value. To determine the exact bottom area of protrusion that will generate the maximum relative bandgap width for PCPs with spherical and cylindrical protrusions, AGA is applied to implement the optimization of relative bandgap width for PCPs with one-side and double-side protrusions. In COMSOL Multiphysics 6.0, the calculation is controlled by MATLAB. In AGA, the cross probability P_m and mutation probability P_c of the genetic algorithm are adjusted adaptively, improving the convergence accuracy and speed. The calculation method of P_m and P_c is:

$$P_m = \begin{cases} 0.1(f_{max} - f)/(f_{max} - \bar{f}), & f' \geq \bar{f} \\ 0.01 \quad , & f' < \bar{f} \end{cases}, \tag{7}$$

$$P_c = \begin{cases} 0.8(f_{max} - f')/(f_{max} - \bar{f}), & f' \geq \bar{f} \\ 0.8 \quad , & f' < \bar{f} \end{cases}, \tag{8}$$

Where f' is the large one in the two individuals participating in the crossover; f is the fitness value of the individuals participating in the mutation; f_{max} is the maximum fitness of the population; and $\bar{f}$ is the average fitness of the population.

For the PCPs with protrusions, the bottom area of the protrusion is taken as the variable of design. It can be seen from Figure 3 and Figure 4 that the gap between each bandgap of the PCPs is no more than 50 Hz, which can be ignored in optimization. Therefore, the relative bandgap width between bandgap curves is selected as the objective function. The formula for calculating the relative bandgap width is:

$$W = \frac{2(\min B - \max A)}{(\max A + \min B)}, \tag{9}$$

Where W is the relative bandgap width, which is the ratio of bandgap width to bandgap center frequency; A represents the characteristic frequency values of the modes on the lower boundary of bandgap; and B represent the characteristic frequency values of the modes on the upper boundary of the bandgap. The design interval of bottom area S is selected from 35 mm^2 to 45 mm^2, as we mentioned above. The results of optimization and the comparison before and after optimization are shown in Table 3 and Table 4, respectively.

Table 3: Results of optimization design.

Protrusion type	Bottom area (mm^2)	The sum of the relative bandgap width	Protrusion volume (mm^3)
One-side sphere	43.71	1.0148	10.62
One-side cylinder	42.54	1.1274	21.27
Double-side sphere	42.08	1.0409	21.24
Double-side cylinder	42.78	1.1857	42.54

Table 4: Comparison of the sum of relative bandgap width before and after optimization.

Protrusion type	Before optimization	After optimization	Increase rate
One-side sphere	0.54	1.02	88%
One-side cylinder	0.73	1.1274	54%
Double-side sphere	0.63	1.0409	65%
Double-side cylinder	0.75	1.1857	58%

According to the optimization results, the model is re-established and calculated, and the bandgaps are obtained, as shown in Figure 7 (right). In the COMSOL software, the solid mechanics module is used to calculate the corresponding frequency response curve further. During the calculation, a 3×3 finite periodic structure is selected, and the X-axis forward excitation is applied to the left side of the structure. The frequency response curve is finally obtained, as shown in Figure 7 (left).

As can be seen from Table 4, the relative bandgap width of the PCPs with one-side spherical protrusion is increased by 88% through optimization. Meanwhile, the volume of the protrusion only increases by 3.5 mm^3. A small growth in the volume of protrusion can improve the bandgap characteristics of the PCPs. The relative bandgap width of PCPs with one-side cylindrical, double-side cylindrical, and double-side spherical protrusion increases by 54%, 58%, and 65%, respectively. As shown in Figure 7, the bandgap characteristics are improved significantly after optimization. The bands over 400 Hz are almost flat, and the interval between adjacent bandgaps is very small and can be neglected. Thereby, broadband can be obtained. The band structures are in good agreement with the frequency response curve, and the attenuation amplitude is large enough to verify the accuracy and effectiveness of the optimization.

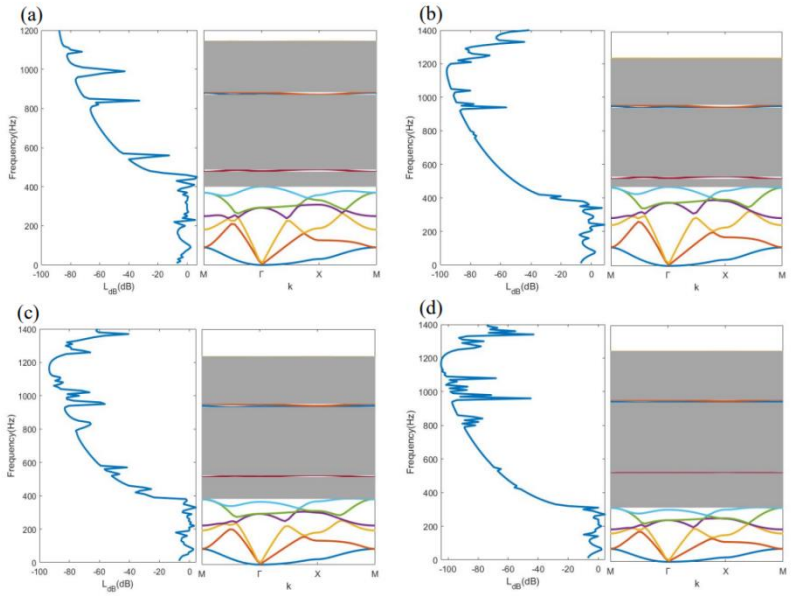

Figure 7: Frequency response curve (left) and band structures (right) of the PCPs with (a) one-side and (b) double-side spherical protrusions; Frequency response curve (left) and band structures (right) of the PCPs with (c) one-side and (d) double-side cylindrical protrusions.

3. Conclusions

In summary, PCPs with three types of protrusions (spherical, square, and cylindrical) are proposed. The band structures of PCPs with both one-side and double-side protrusions are calculated numerically. The results show that the addition of protrusions on PCPs could result in lower local resonance. The influences of all geometric and material parameters on the band structures are analyzed, and the bottom area of the scatterer is selected as the key decision variable. Then, the optimization is implemented to get an optimal relative bandgap width with an adaptive genetic algorithm. Finally, the structures with optimal bandgap characteristics are obtained. Compared with the original structures presented in Figure 1, the relative bandgap width of the optimized PCP with one-sided spherical protrusions is increased by 88%. Similarly, the relative bandgap widths of PCPs with one-side cylindrical, double-side spherical, and double-side cylindrical protrusion PCPs are increased by 54%, 65%, and 58%, respectively. The studies try to broaden the application of PCPs in vibration damping and noise reduction, with smaller volume and significantly improved band gap characteristics, and provide a new idea for lightweight vibration insulation materials.

References

[1] M. Addouche, M. A. Al-Lethawe, A. Choujaa, and A. Khelif. (2014) Superlensing effect for surface acoustic waves in a pillar-based phononic crystal with negative refractive index,Applied Physics Letters, 105, 023501.
[2] Z. Tan, Y. Wei, Y. Tian, and X. Han. (2019) Gradient negative refraction index phononic crystal lens with a rotating scatterer, Materials Research Express, 6, 096203.
[3] F. Yang, Z. Tan, X. Han, and C. Cho. (2021) A graded negative refraction-index phononic crystals plate lens for focusing A0 mode Lamb wave and energy harvesting. Results in Physics, 31, 105006.
[4] X. Zhang and Z. Liu. (2004) Negative refraction of acoustic waves in two-dimensional phononic crystals, Applied Physics Letters, 85, 341.
[5] J. Han, S. Tang, R. Wang, and W. Wang. (2019)Acoustic wave transmission channel based on phononic crystal line defect state, AIP Advances, 9, 065201.
[6] H. Liu, T. Liu, L. Song, Q.-M. Zhang, Y.-X. Fan, and Z.-Y. Tao. (2021) Temperature tuning of defect state induced by the periodic cavities between the phononic crystals,AIP Advances, 11, 075113.
[7] X. P. Wang, P. Jiang, T. N. Chen, and K. P. Yu. (2016) Frequency characteristics of defect states in a two-dimensional

phononic crystal with slit structure. International Journal of Modern Physics B, 30, 1650025.
[8] L. Chen, Y. Guo, and H. Yi. (2021) Optimization study of bandgaps properties for two-dimensional chiral phononic crystals base on lightweight design. Physics Letters A, 388, 127054.
[9] Z. Guo, S. Chen, C. Wang, and C. Hao. (2022) Subwavelength bandgap phononic crystals with mixed resonant modes. Physics Letters A, 438, 128109.
[10] D.-H. Han, G.-J. Zhang, J.-B. Zhao, and H. Yao. (2022) Study on bandgap of a novel phononic crystal with low-frequency sound insulation, AIP Advances, 12, 055329.
[11] S. Li, Y. Dou, T. Chen, J. Xu, B. Li, and F. Zhang. (2019) Designing a broad locally-resonant bandgap in a phononic crystals, Physics Letters A, 383, 1371-1377.
[12] W. Li, F. Meng, Y. f. Li, and X. Huang. (2019) Topological design of 3D phononic crystals for ultra-wide omnidirectional bandgaps, Structural and Multidisciplinary Optimization, 60, 2405-2415.
[13] G.-G. Xu, X.-W. Sun, R.-S. Li, Z.-R. Zhang, T. Song, and Z.-J. Liu. (2021) The low-frequency bandgap characteristics of a new three-dimensional multihole phononic crystal, Applied Physics A, 127, 812.
[14] M. M. Sigalas and E. N. Economou. (1992) Elastic and acoustic wave band structure, Journal of Sound and Vibration, 158, 377-382.
[15] Z. Liu, X. Zhang, Y. Mao, Y. Y. Zhu, Z. Yang, C. T. Chan, and P. Sheng. (2000) Locally Resonant Sonic Materials, Science, 289, 1734-1736.
[16] Y. Pan, R. Liu, G. Bin, and X. He. (2022) Vibration and noise reduction of phononic crystal structure laid on the noise transmission path of axial piston pump, Applied Acoustics, 200, 109075.
[17] Y. Ruan, X. Liang, X. Hua, C. Zhang, H. Xia, and C. Li. (2021) Isolating low-frequency vibration from power systems on a ship using spiral phononic crystals, Ocean Engineering, 225, 108804.
[18] B. Zhang, P. Chen, H. Chen, T. Feng, C. Cai, and J. Zhang. (2021) Application of phononic crystals for vibration reduction and noise reduction of wheel-driven electric buses based on neural networks, Proceedings of the Institution of Mechanical Engineers, Part D: Journal of Automobile Engineering, 236, 1619-1627.
[19] W. J. SONG Yubao, YU Dianlong. (2018) Review of vibration and noise contral of the plate structures, Journal of Mechanical Engineering 54, 60-77.
[20] W. J. Y. D. W. Gang and Z. H. L. Yaozong. (2005) Theory and experimental investigation of flexural wave propagation in thin rectangular plate with periodic structure, Chinese Journal of Mechanical Engineering, 18, 1.
[21] J. O. Vasseur, P. A. Deymier, B. Djafari-Rouhani, Y. Pennec, and A. C. Hladky-Hennion. (2008) Absolute forbidden bands and waveguiding in two-dimensional phononic crystal plates, Physical Review B, 77, 085415.
[22] Z. J. Yao, G. L. Yu, and J. B. Li. (2011) Flexural Vibration Band Gaps in a Ternary Phononic Crystal Thin Plate, Materials Science Forum, 675-677, 1085-1088.
[23] H.-F. Zhu, X.-W. Sun, T. Song, X.-D. Wen, X.-X. Liu, J.-S. Feng, and Z.-J. Liu. (2021) Tunable characteristics of low-frequency bandgaps in two-dimensional multivibrator phononic crystal plates under prestrain, Scientific Reports, 11, 83-89.
[24] H.-y. Yang et al.. (2023) Low frequency elastic waves and vibration control mechanism of innovative phononic crystal thin plates, Physica B: Condensed Matter, 667, 415189.
[25] Y. Jin, Y. Pennec, Y. Pan, and B. Djafari-Rouhani. (2017) Phononic crystal plate with hollow pillars connected by thin bars, Journal of Physics D: Applied Physics, 50, 035301.
[26] Y. Pennec, B. Djafari-Rouhani, H. Larabi, J. O. Vasseur, and A. C. Hladky-Hennion. (2008) Low-frequency gaps in a phononic crystal constituted of cylindrical dots deposited on a thin homogeneous plate, Physical Review B, 78, 104105.
[27] T.-T. Wu, Z.-G. Huang, T.-C. Tsai, and T.-C. Wu. (2008) Evidence of complete band gap and resonances in a plate with periodic stubbed surface, Applied Physics Letters, 93, 111902.
[28] H.-J. Zhao, H.-W. Guo, M.-X. Gao, R.-Q. Liu, and Z.-Q. Deng. (2016) Vibration band gaps in double-vibrator pillared phononic crystal plate, Journal of Applied Physics, 119, 014903.
[29] Y. Li, J. Chen, X. Han, K. Huang, and J. Peng. (2012) Large complete band gap in two-dimensional phononic crystal slabs with elliptic inclusions, Physica B: Condensed Matter, 407, 1191-1195.
[30] K. Yu, T. Chen, and X. Wang. (2013) Band gaps in the low-frequency range based on the two-dimensional phononic crystal plates composed of rubber matrix with periodic steel stubs, Physica B: Condensed Matter, 416, 12-16.
[31] K. Wang, Y. Liu, and B. Wang. (2019) Ultrawide band gap design of phononic crystals based on topological optimization, Physica B: Condensed Matter, 571, 263-272.
[32] X. K. Han and Z. Zhang. (2019) Topological Optimization of Phononic Crystal Thin Plate by a Genetic Algorithm, Scientific Reports, 9, 8331.
[33] C. Xiong, C.-Y. Lee, and Q.-H. Qin. (2023) Topology optimization of single-phase phononic crystals based on a search-space-reduction strategy with a Genetic Algorithm, Materials Today Communications, 34, 105069.
[34] W. Li, G.-G. Wang, and A. H. Gandomi. (2021) A Survey of Learning-Based Intelligent Optimization Algorithms, Archives of Computational Methods in Engineering, 28, 3781-3799.
[35] X. Wen, L. Kang, X. Sun, T. Song, L. Qi, and Y. Cao. (2023) Topological Design of Two-Dimensional Phononic Crystals Based on Genetic Algorithm, Materials,16.
[36] L. Xie, B. Xia, J. Liu, G. Huang, and J. Lei. (2017) An improved fast plane wave expansion method for topology optimization of phononic crystals, International Journal of Mechanical Sciences, 120, 171-181.